journal of the mechanical behavior of biomedical materials 133 (2022) 105306

Contents lists available at ScienceDirect

Journal of the Mechanical Behavior of Biomedical Materials

journal homepage: www.elsevier.com/locate/jmbbm

Nanoindentation and nano-scratching of hydroxyapatite coatings for resorbable magnesium alloy bone implant applications

Patrick Lemoine [a,*], Jonathan Acheson [a], Stephen McKillop [a], Jeroen JJP. van den Beucken [b], Joanna Ward [a], Adrian Boyd [a], Brian Meenan [a]

[a] Nanotechnology and Integrated Bioengineering Centre (NIBEC), School of Engineering, Ulster University, United Kingdom
[b] Regenerative Biomaterials, Dentistry, Radboud UMC, NL-6525, EX, Nijmegen, the Netherlands

ARTICLE INFO

Keywords:
Hydroxyapatite
Resorbable bone implant
Magnesium alloy
Nanoindentation
Nanotribology

ABSTRACT

The corrosion rate of Mg alloys is currently too high for viable resorbable implant applications. One possible solution is to coat the alloy with a hydroxyapatite (HA) layer to slow the corrosion and promote bone growth. As such coatings can be under severe stresses during implant insertion, we present a nano-mechanical and nano-tribological investigation of RF-sputtered HA films on AZ31 Mg alloy substrates. EDX and XRD analysis indicate that as-deposited coatings are amorphous and Ca-deficient whereas rapid thermal annealing results in c-axis orientation and near-stoichiometric composition. Analysis of the nanoindentation data using a thin film model shows that annealing increases the coating's intrinsic hardness (H) and strain at break (H/E) values, from 2.7 GPa to 9.4 GPa and from 0.043 to 0.079, respectively. In addition, despite being rougher, the annealed samples display better wear resistance; a sign that the rapid thermal annealing does not compromise their interfacial strength and that these systems have potential for resorbable bone implant applications.

1. Introduction

Surgical procedures to remove metallic bone implants present infection risks, significant in the current climate, considering the global antimicrobial issue affecting the management of nosocomial infections. They also represent risks inherent to anaesthesia. Hence, much research is being conducted on developing alternatives involving resorbable metallic bone implants where, ideally the implant is being corroded by the body at the same rate of the bone regrowth (i.e., the resorption). One often explored material is magnesium (Yoshizawa et al., 2014) and its alloys for three reasons. Magnesium has a Young's modulus (~40 GPa) much closer to that of bone (~20 GPa) than metals traditionally used for implants (steel ~ 200 GPa, Ti alloys ~ 150 GPa), therefore reducing the effects of stress shielding. Magnesium is bioactive and can facilitate the growth of osteoblast cells (He et al., 2016), and as such has been included in bone cement formulations (Lilley et al., 2005) or implanted in titanium surfaces to improve the response of human bone marrow derived mesenchymal stem cells (Won et al., 2017). This also means that eventual Mg wear debris, from the implant insertion or from its repeated mechanical loading in the body, are less likely to release allergic/toxic ions from Ni, Cr or Co or cause inflammation or osteolysis, as it has been observed for traditional orthopaedic implants made from stainless steel, Co- or Ti-alloys (Markhoff and Grabow, 2020; Borcherding et al., 2021). Finally, magnesium has a low electrode potential (−2.37 V) and corrodes easily when exposed to body fluids. Indeed, the main challenge to the development of useable magnesium alloy resorbable bone implants is the control of the magnesium corrosion rate. Some researchers have postulated a desired value of 0.5 mm/year in simulated body fluid at 37 °C (Yan et al., 2021) to match the bone regrowth rate, although the notion of an ideal value is somewhat debatable as the corrosion rate can be different when the surrounding tissue is bone or muscle (Antoniac et al., 2021). What is obvious is that, at present Mg alloys corrode too fast. This issue has been addressed by adjusting the composition of the Mg alloy, for instance using extraluminal tracheal stent prepared from a magnesium-yttrium alloy (Luffy et al., 2014), but unfortunately without sufficient improvement in corrosion resistance. Decreasing the extrusion temperature of Mg–Zn–Ca-(Mn) alloys caused grain refining which improved both the mechanical properties and the corrosion resistance of these alloys (Bazhenov et al., 2021). Another interesting strategy is the preparation of honey-combed graphene oxide (GO)-Mg alloy composite where the GO finely dispersed within the composite, again improving its mechanical properties and protecting its Mg grain boundaries against

* Corresponding author.
E-mail address: p.lemoine@ulster.ac.uk (P. Lemoine).

https://doi.org/10.1016/j.jmbbm.2022.105306
Received 22 March 2022; Received in revised form 12 May 2022; Accepted 30 May 2022
Available online 7 June 2022

corrosion (Shuai et al., 2019). An alternative solution, examined in the present paper and compatible with more widely available and processable commercial Mg alloys, is to coat the alloy with a thin film of hydroxyapatite (HA), to slow down corrosion, act as a barrier layer but also promote bone growth as HA is bioactive and can be osteoinductive. We have addressed the issue of corrosion rate measurements on those coated alloys in previous studies (Acheson et al., 2019, 2021). However, coating an implant device brings its own issues as shear and compressive stresses can damage the coating during the insertion process. Indeed, in a recently published study, we determined the interfacial shear strength of calcium phosphate coatings on magnesium alloy double-lap shear joints using shear testing and modelling their failure with FEA analysis (Acheson et al., 2022). An alternative method of testing the coating/substrate bond is to use practical wear tests, as developed for industrial coatings, generally consisting of a hard counterbody sliding against the coated sample while a ramping normal load is applied. Here again FEA modelling of the experiment must be conducted to extract the interlaminar shear strength. These wear tests also allow for investigation of ploughing, by measuring wear rate or load at failure in constant load tests which is useful as the ploughing of the coating can be a contributing factor in implant failure. Overall, these wear tests are useful to compare coating's expected performance on insertion but they only give semi-quantitative information on the behaviour of coated implants during implantation, because orthopedic implants such as surgical screws, plates and Kirschener wires have complex geometries not mimicked by the wear test. Therefore, ultimately, only FEA analysis can predict the implant behaviour on insertion and this requires the knowledge of the interlaminar shear strength, already discussed, but also of the coating's Young modulus (E), which cannot be easily determined by traditional tensile or bending tests on macroscopic coated specimen. However, the E value of the coating can be determined by nanoindentation. Nanoindentation also determines the coating's hardness (H) value, which relates to its yield strength, a parameter also required for the FEA modelling. In addition, this technique measures these E and H values at the local scale, spotting eventual variations in properties, whereas traditional mechanical testing techniques only give average values over macroscopic dimensions. Hence, the aim of the present work is to carry out a nanoindentation and nano-scratch testing investigation on RF-sputtered HA coating deposited onto AZ31 Mg alloy substrate with complementary analysis from atomic force microscopy (AFM), field emission scanning electron microscopy (FESEM), Energy dispersive X-ray spectroscopy (EDX) and X-ray diffraction analysis (XRD). Its objective is to obtain the E and H values as well as the wear rate and critical load for delamination (L_c). To date only two similar studies have been published. One paper discusses nanoindentation of RF magnetron coated HA coatings on Mg alloy (Surmeneva et al., 2015) and another provides a macroscopic (R = 6 mm ball-on-disc tribological study of similar coatings (Dinu et al., 2017), however, to the best of our knowledge there are no published nanotribological investigation of such coatings. The present investigation has two distinct advantages. Firstly, it uses a small tip radius R and produce shear stresses generally close to the film/substrate interface and hence these experiments are better adapted to investigate the film/substrate region that traditional wear tests using larger tip radius. Secondly, the nanoindentation experiments use continuous stiffness measurements (CSM) and a film's model to extract intrinsic film's E and H values, something not attempted to date on these coatings. Hence the aim of the study is the determination of the aforementioned nano-tribological parameters. The follow-up study which consists in using these parameters to conduct an FEA analysis of the implantation is beyond the scope of the present work and will be the object of a forthcoming publication.

2. Materials and methods

The magnesium alloys investigated in this work are commercial grade AZ31 alloys of nominal composition: 96% Mg, 3% Al, 1% Zn (Goodfellow, UK). As nano-mechanical and nano-tribological analysis are affected by topography and indeed require smooth surfaces to give an accurate estimation of the relevant parameters discussed above, AZ31 specimen were cut in coupons of size 10 mmx 10 mm x 1 mm and polished using a Struers TegraPol-31 mechanical polisher. Magnesium alloys are soft and hygroscopic and consequently challenging to polish. The protocol employed here was to manually polish the coupons with P1200, then P4000 SiC paper (RS-Components UK) and finally abraded using a 1 μm diamond paste using isopropyl alcohol as a lubricant and a rinsing aid. Unless specified otherwise, all AZ31 referred to in this publication have been fine-polished, as described above.

The HA films were deposited by an RF (13.56 MHz) magnetron sputtering system (Kurt J. Lesker, USA) using targets prepared by dry pressing 11.5 g of medical grade Captal "R" Hydroxyapatite (HA) (Plasma Biotal, UK) into a recessed copper disk using a stainless-steel die compressed to a load of 80 kN for 60 s. The depositions were performed, typically using 150 W power, 5×10^{-5} bar chamber pressure and argon as a working gas, described in detail previously (Acheson et al., 2019, 2021; Boyd et al., 2013). To define the relationship between deposition time and film thickness, a protocol was established based on the use of Time-of-Flight Secondary Ion Mass Spectrometry (ToF-SIMS) and contact profilometry. The ToF-SIMS system (ToF-SIMS 5 instrument from IONTOF GmbH, Germany) uses a 25 keV Bi^+ primary beam and analysis was set to detect positive ions. Depth profiling was performed using a Cs^+ secondary ion beam operating at an energy of 10 keV. The ToF-SIMS sputtering was carried out up to the crossover point between Ca^{2+} and Mg^{2+} ions after which the depth of the trench was measured via contact profilometry using a Dektak XT stylus profilometer (Bruker, Germany). Based on previous work where HA films were deposited on AZ31 coupons polished with P1200 SiC paper (Acheson et al., 2019, 2021), this analytical protocol gave thicknesses of 370 nm and 1340 nm thickness, for deposition times of 30 and 100 h, respectively called H30 and H100. These deposition times are considerably longer than for deposition on titanium substrates as the deposition rate tends to be smaller on magnesium. One should note that these values are only approximate, indeed for smoother surfaces (1 μm diamond paste polish), the deposition rates may be slightly smaller.

Finally, as it is usually expected that *as received* RF magnetron sputtered HA films prepared at moderate power are amorphous, annealing by heat treatment is a recognised method to control the solubility of HA coating in simulated body fluids and hence to regulate their bioactivity. However, with a magnesium alloy substrate, this cannot be carried out in a conventional oven but can be successfully achieved using flash-annealing and an IR source (Yuan et al., 2010; Yoshinari et al., 1997). In this work, we used a Quad Ellipse Chamber (Model E4-10-P, Research MN). Sample H100-A1 was treated once to ~600 °C for 15s. Sample H100-A2 was treated twice to ~600 °C for 15s, without intermediate cooling down (i.e., effectively 30 s). Based on previous works by co-author Jeroen JJP van den Beucken (Takahashi et al., 2008; Fernandes et al., 2017), it was shown that these parameters were adequate to crystallise HA films of ~1 μm thickness.

X-ray diffraction (XRD) analysis of the films and substrate was carried out in the θ−2θ configuration using a 3rd generation Empyrean XRD analysis system (Malvern Panalytical Ltd, UK) operating at 45 KV and 30 mA using a Cu Kα1 radiation (λ = 1.5406 Å). The peaks observed in the XRD patterns were indexed using peak positions from the International Center for Diffraction data, file ICDD #01-071-5048 for the hcp phase of hydroxyapatite and file ICDD#00-035-0821 ofr the α-Mg phase in the AZ31 Mg alloy.

The topography of the AZ31 substrates and coatings was analysed with tapping AFM microscopy (TAFM) with a Bruker AFM 3100 system (Bruker, Germany) operated at a high tapping set point amplitude using a TESPA cantilever (nominal k~40 N/m and f~300 kHz). FESEM microscopy was carried out with a Hitachi SU5000 system (Hitachi, Japan) in a range of conditions (2–10 kV, SE and BSE detection, low and high vacuum) to maximize surface sensitivity or compositional contrast, as

required. Image J was then used to analyse surface features seen on the AFM and FESEM micrographs using a particle analysis protocol based on scaled, cropped and binarized micrographs.

EDX analysis used an Aztec system with an X-max 80 silicon drift EDX detector (Oxford Instruments, UK) using electron accelerating voltages varying from 2 kV to 10 kV, again to maximize surface or atomic sensitivity. Considering the relatively weak X-ray absorption into the HA film for the relevant X-ray energy range, this surface sensitivity is mainly influenced by the electron rage R_{KO}, which can be estimated using the Kanaya-Okayama formula (Kanaya and Okayama, 1972)

$$R_{KO} = 0.0276.A.\frac{E_o^{1.67}}{\rho.Z^{0.89}} \quad (1)$$

where A is the average atomic mass of the HA film (in g/mol), E_o is the primary electron energy (in keV), ρ is the HA film density (in g/cm^3) and Z is the HA film's average atomic number. The value of A and Z were calculated using a weight-averaged rule of mixture (Howell et al., 1998; Muller, 1954).

The nanomechanical and nanotribological properties of the samples were measured using a NanoIndenter XP system (Keysight Technologies, USA) with a load and displacement resolutions of 1 nN and 0.1 nm, respectively. The nanoindentation protocol followed in this study results from many years of depth sensing indentation on a variety of thin film systems and covers most aspects defined in the nanoindentation standard ISO 14577–1:2015. These measurements were done using a Berkovitch diamond tip (semi-included apex angle = 65.27°). Each sample was characterised with an array of 16 indents made 30 μm apart, the tip calibration was performed using the Oliver and Pharr model (Oliver and Pharr, 1992) on smooth fused silica flats to determine the tip area function and the system's load frame compliance. As the response of coated systems depends on the film's and substrate properties, film thickness and depth (Lemoine et al., 2000, 2007), the measurements were carried out in depth control mode up to 2000 nm depth, at a constant strain rate of 0.1 s^{-1}, using the continuous stiffness measurements (CSM) option, giving Young's modulus (E) and hardness (H) values as a function of indentation depth h. Surface contact was detected by a stiffness change set at 200 N/m, which for stiff inorganic materials (~E* = 100 GPa) correspond to a 1 nm Hz contact radius, hence a very small deformation of the surface. On surface contact detection, the loading was only initiated once the measured drift rate was below 0.05 nm/s. A hold segment was also positioned after the unloading to correct for residual drift. As indentation proceeds, one can distinguish qualitatively three regions; a shallow depth/surface region dominated by the blunted geometry of the tip apex, an intermediate depth/film region influenced by the film properties and a large depth/substrate region where the properties of the substrate strongly affect the system's response. However, delimitation of these three regions is difficult. Instead, the film's intrinsic properties can be extracted from the response of the coated system using a phenomenological approach, as that of the Bhattcharya model (Bhattcharya and Nix, 1998), based on finite element analysis (FEA) modelling. For a hard film (HA) on a soft substrate (AZ31 Mg alloy), the hardness of the coated system H is;

$$H = H_S + (H_F - H_S).\exp(-k_1.\beta_c) \quad (2)$$

where H_S and H_F are, respectively the substrate's and film's hardness, k_1 is a constant and β_c is the ratio of contact depth h_c over film thickness t. Similarly, the measured modulus of the coated system E can be defined as;

$$E = E_S + (E_F - E_S).\exp\left(-k_2.\beta_e^{\frac{1}{2}}\right) \quad (3)$$

where E_S and E_F are, respectively the substrate's and film's moduli, k_2 is a constant and β_e is the ratio of elastic depth over film thickness. The elastic depth can be calculated from the contact depth h_c; $h_e = 2\ (h\text{-}h_c)$, where h is the full depth.

Nano-scratch testing was carried out with a procedure previously used in our laboratory (Lemoine et al., 2004) and similar to that employed in many other thin film studies (Banday et al., 2021; Zhi et al., 2022; Ma et al., 2021). Compared to the nanoindentation study, we used a more acute diamond cube corner tip (semi-included apex angle = 45°) to increase strain and trigger brittle fracture. Constant load experiments permitted the study of the wear resistance of the coatings, whilst ramping load experiments allowed the investigation of coating delamination. For both set of experiments, the scratching was done in the edge-forward and face-forward directions and the pre-scratch and post-scratch segments were done at a topographic load of 20 μN normal load. For the ramping load experiments, preliminary tests established that a final ramping load of 20 mN was adequate for all HA coatings. The constant load experiments used loads of 0.5, 1 and 2 mN. The scratching speed v varied from v = 1 μm/s to v = 10 μm/s. Considering that these experiments produced scratches with widths w varying from w = 1 to w = 2 μm, this gives strain rates during scratching ε' = dε/dt (=v/w) varying from 0.5 to 1 s^{-1} (for v = 1 μm/s) and 5-10 s^{-1} (for v = 10 μm/s). According to a previous study on the strain rate sensitivity of scratched HA films (Ahmed and Jankowski, 2011), this range of strain rates result in a strain rate sensitivity of −0.058, hence very little change in scratch response. For all scratch experiments, the scratches were analysed by SEM/EDX analysis and EDX mapping to help identify HA and Mg regions and corroborate the data obtained by the scratch profiles (Lemoine et al., 2004).

Finally, for all quantitative measurements, average values are given with error bars representing the standard error of the mean over the measurements. The statistical analysis of the data was done using Microsoft Excel and a student t-test was implemented to make pair comparisons. The p-value were calculated assuming equal variance for both and using two tails. All results are discussed in term of statistically significant differences for p-value < 0.05.

3. Results and discussion

3.1. Morphological, compositional and structural analysis results

The SEM/EDX data shown in Fig. 1 clearly indicates that, going from the P4000 SiC paper polish to the 1 μm diamond paste polish, the surface morphology of the AZ31 Mg alloy becomes much smoother, and this outlines the compositional contrast in small micron-size regions of high Z number material; the β $AlMn_5$ phase as evidenced from the EDX maps and as expected for a AZ31 alloy (Esmaily et al., 2017).

The TAFM micrographs shown in Fig. 2 confirm that this last stage of polishing with the diamond paste brings the most significant change in surface morphology, with roughness values down from several 100 nm to below 20 nm; a greatly improved scenario for undertaking nano-indentation and nano-scratching measurements.

Surface-sensitive 2 kV-high magnification FESEM micrographs of the coated samples are shown in Fig. 3. The H30 and H100 films display a similar globular nanostructure with spheroid grains of approximately 100–200 nm diameter (Fig. 3(b and c)), not present on the fine-polished (R_a^{AZ31} = 10 nm) uncoated AZ31 substrate (Fig. 3(a)) on which those coatings were deposited. Previous studies of RF magnetron sputtered HA films showed very similar nanostructure (Surmenev et al., 2011; Surmeneva et al., 2014). In Fig. 3 (d) is shown another H100 sample deposited on a rough-polished HA-coated substrates (up to P1200 SiC grit; R_a^{AZ31} = 300 nm), displaying again the same nanoscale morphology as seen on the H30 and H100 sample of Fig. 3 (b, c). Therefore, the nano-morphology of the HA coating is not influenced by the substrate's topography. Fig. 3(e and f) indicates that, upon annealing (samples H100-A1 and H100-A2), this regular surface nanostructure disappears with similar bright nodules appearing on the surface of both annealed samples.

EDX analysis of the samples is presented in Table 1 for a 5 kV electron

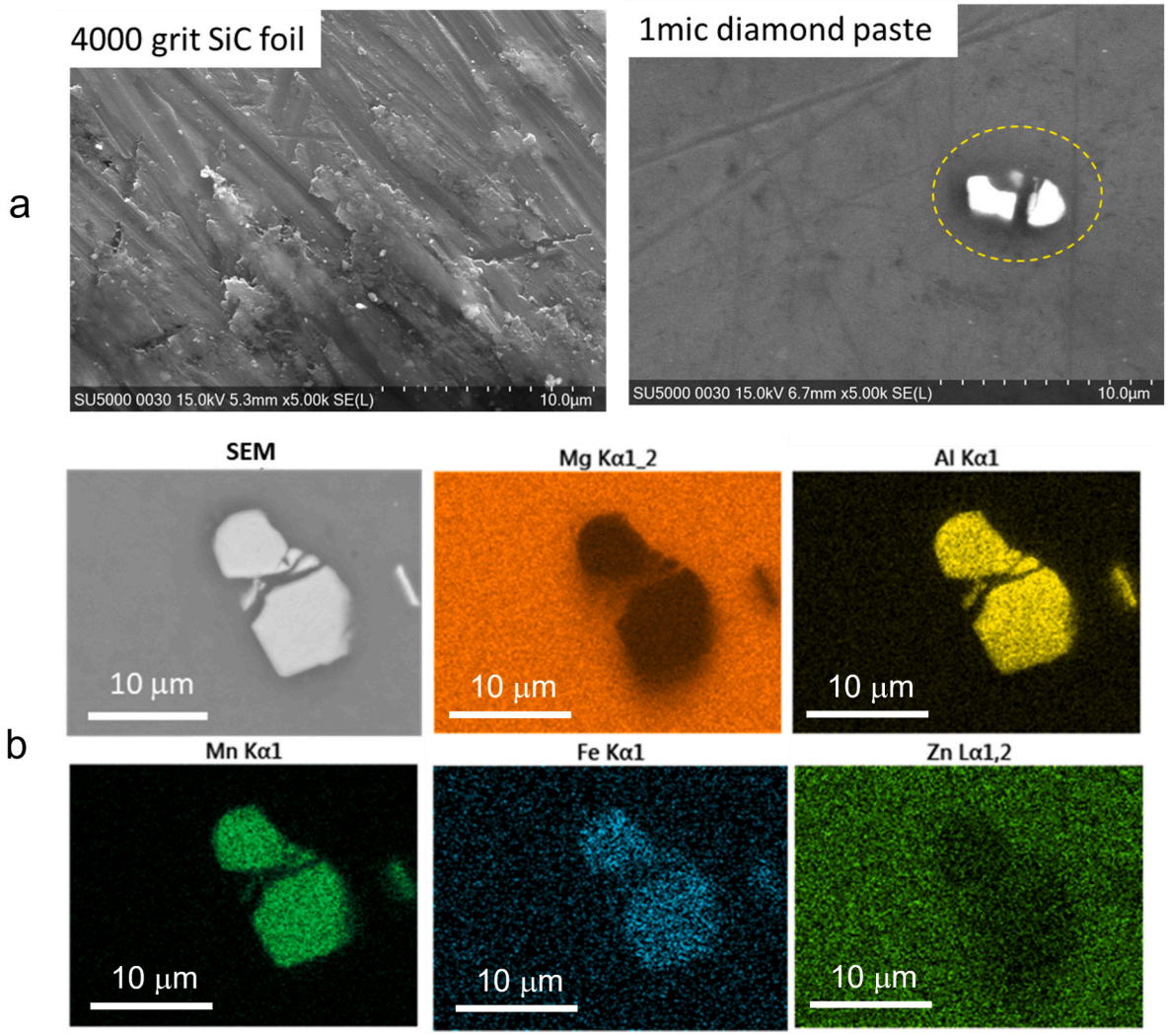

Fig. 1. (a) FESEM micrographs of AZ31 Mg alloy substrates polished with P4000 SiC foil and 1 μm diamond paste (b) EDX maps showing the presence of a micron-size $Al_6Mn_5(Fe)$ phase (β) segregation, also shown in (a) with the dashed oval.

energy, giving an R_{KO} value of 686 nm, smaller than the film thickness, with enough atomic sensitivity to detect most of the relevant peaks yet giving enough surface sensitivity to confine the analysis to the HA film region. We note that, from the student t-test analysis of p-values for the pair comparisons of Ca/P ratio between samples, that the H100 sample is calcium deficient whereas the annealed samples have a similar near-stoichiometric composition. It is indeed generally found that film deposition techniques using multi-elemental targets, like laser ablation deposition or RF magnetron sputtering, do not always reproduce faithfully the stoichiometry of the target in the film. This is because these film deposition processes are essentially non-equilibrium unless a significant source of energy is supplied as substrate heating or simply using a large laser or RF power. It is therefore often observed that HA film deposited by RF magnetron sputtering, using low RF power have a non-stoichiometric composition (Surmenev, 2012). Flash-annealing the film provides the extra energy resulting in the equilibrium stoichiometry, i.e. with a Ca/P ratio close to 1.6.

Fig. 4 shows the XRD scans of the films. Peaks from the α-Mg phase present in the underlying AZ31 substrate can be seen at 32.193° (100), 34.398° (002) and 36.619° (101) whereas peaks from the hexagonal-close-packed (hcp) HA phase would be seen at 25.864° (002) and ~31.758° (211) and 32.178° (112)). An XRD scan of an AZ31 Mg substrate, not shown here, indicates that the peak intensities of the α-Mg peaks are similar in the H100 sample and the AZ31 Mg substrate, indicative of the X-ray transparency of the films (from NIST database; X-ray absorption depth = 19 μmat λ = 0.154 nm). One also observes that the *as-received* H100 sample displays no HA peak, hence is probably amorphous. Previous studies have indeed shown that unannealed HA films prepared by magnetron sputtering are generally amorphous, unless prepared with high power (>500W) and/or a negative substrate bias which both increase the plasma density and hence, the *in situ* deposition temperature (Acheson et al., 2021; Surmeneva et al., 2014). By contrast, the flash-annealed samples H100-A1 and H100-A2 display a peak from the hcp HA phase at at 25.864° (002). This hcp phase has also peaks at 31.758° (211) and 32.178° (112), which overlap with the α-Mg (100) peak at 32.193°. Considering the similar intensities for this peak around 32° for the spectrum of AZ31, H100 and the annealed samples, it is probable that this peak's main contribution is the α-Mg reflection. Hence, the annealed samples only display the (002) hcp HA reflection and, therefore, have a c-axis orientation. One also notes that the intensity of the (002) HA peak observed in samples H100-A1 and H100-A2 is much lower (i.e., 10x counts multiplication in Fig. 4 than those of the α-Mg peaks. This may be indicative of an incomplete crystallization of the films in this flash annealing process. On the other hand, we do not detect any difference in this HA hcp (002) between the XRD patterns of the two annealed samples.

TAFM micrographs of the HA films are shown in Fig. 5 for 5, 10 and 20 μm scans. These micrographs corroborate the FESEM observations,

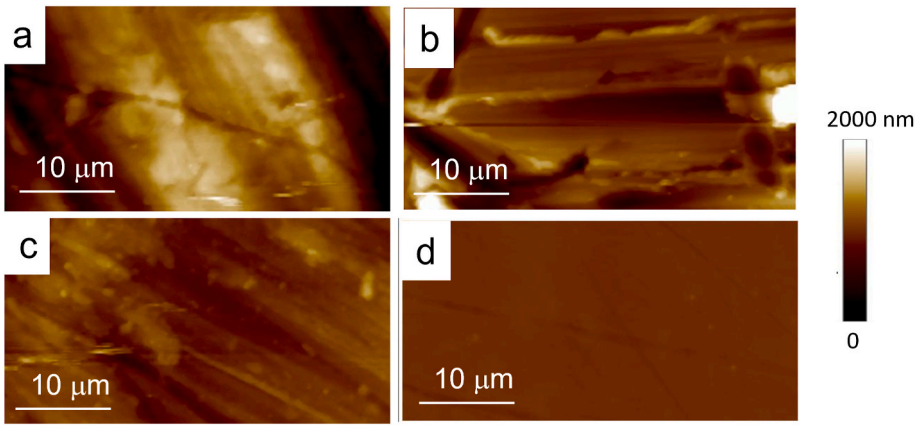

material	R_q, nm	R_a, nm	ΔA/A, %
as rec	380	304	4.15
P1200	282	189	7.73
P4000	137	110	2.5
1 mic. dia.	12.8	9.5	0.14

Fig. 2. 40 μm wide TAFM micrographs of AZ31 Mg alloy substrates; as received (a) and polished with P1200 SiC foil (b), 4000g SiC foil (c) and (d) 1 μm diamond paste. The table gives RMS (Rq) and arithmetic roughness (Ra) values as well as the specific surface area increase. The micron bar is 10 mm, valid for all micrographs.

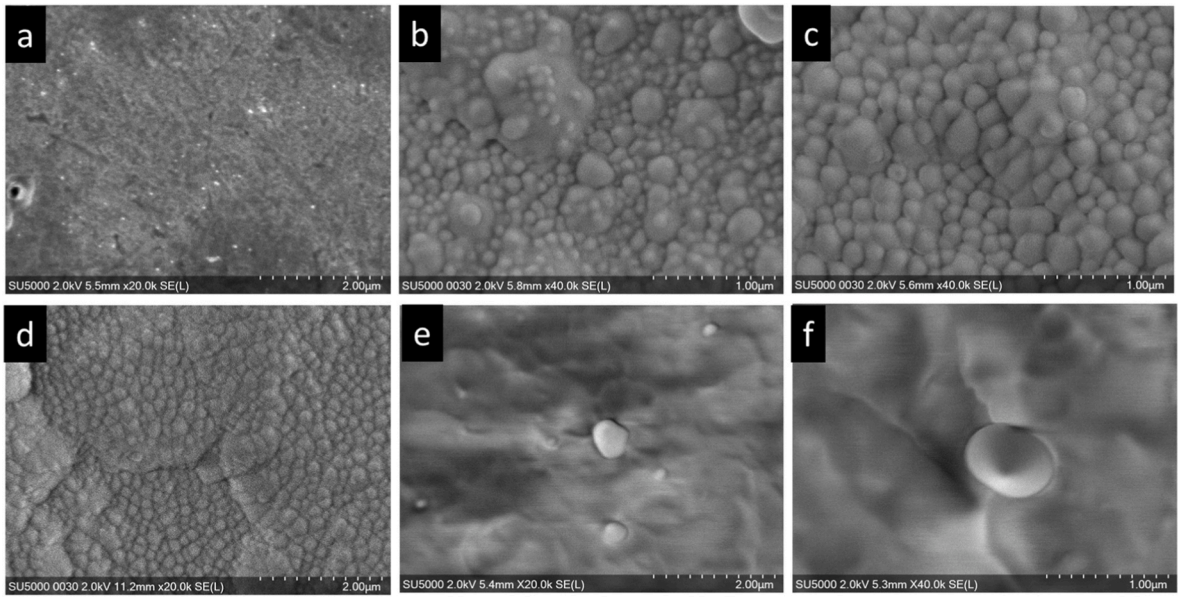

Fig. 3. Low kV 20k-40k FESEM micrographs of a AZ31 Mg alloy surface polished with 1 μm diamond paste (R_a^{AZ31} = 10 nm), (a) uncoated and coated with (b) H30, (c) H100, (e) H100-A1 and (f) H100-A2. A H100 coating on a AZ31 Mg alloy rough-polished with P1200 (R_a^{AZ31} = 300 nm) is shown in (d).

Table 1
EDX composition of the samples deposited for 100 h, obtained at 5 kV energy.

	H100	H100-A1	H100-A2
O	52.48 ± 0.49	54.32 ± 0.61	52.96 ± 0.66
Ca	17.32 ± 0.85	22.30 ± 0.62	20.46 ± 0.85
Ca	16.00 ± 0.43	8.76 ± 0.28	12.62 ± 0.42
P	12.9 ± 0.10	13.32 ± 0.18	12.82 ± 0.40
Mg	1.98 ± 0.11	1.04 ± 0.13	0.55 ± 0.06
Ca/P	**1.33 ± 0.06**	**1.68 ± 0.06**	**1.57 ± 0.11**

the H30 and H100 films display a nano-globular film structure, which disappear upon annealing (samples H100-A1 and H100-A2). The bar charts display statistical analysis of the film's surface topography. The roughness values (R_q and R_a) increase with deposition time/film thickness and upon annealing, however, the specific surface area (ΔA/A, %) does not follow any particular trend. The bar charts also display skewness and kurtosis, useful statistical parameters to describe non-gaussian surface height distributions, particularly important for assessing tribological properties. Surfaces rich in asperities correspond to high kurtosis values (K>3) and positive skewness values (S>0) and it has been shown that such surfaces result in local stress concentration and poor

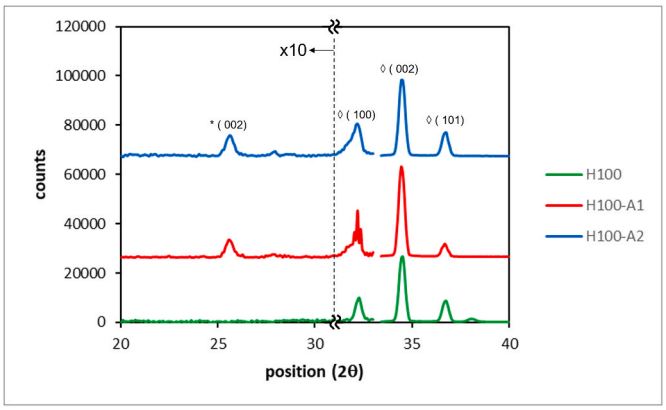

Fig. 4. XRD scan for the H100, H100-A1 and H100-A2 samples. The peaks labelled * are identified as the HA hexagonal phase (counts x10) whereas peaks labelled ⋄ are α-Mg phase present in the AZ31 Mg alloy substrate.

tribological properties (Surmenev, 2012; Kennedy et al., 2003). In the present case, it would seem that these asperities develop during deposition but are somehow mitigated upon annealing. Comparing now the two annealed samples, these TAFM micrographs indicates that the small globules see on the FESEM micrographs are again seen on the TAFM micrographs from both samples and no significant differences between these two samples can be observed.

3.2. Nanoindentation and nano-scratch results

Fig. 6 shows the nanoindentation data for a 1 μm diamond polished AZ31 Mg alloy substrate and the H100 film deposited on it, displaying load-displacement (L-d) curve (Fig. 6 (a)) and the E(h) and H(h) curves (Fig. 6 (b). These L-d curves do not present pop-in events or brittle fractures in the loading segment, this is indicative of a significant plastic deformation behaviour. The sizeable error bars are caused by the significant surface roughness which result in ill-defined contact areas, hence adversely affects the accuracy and reproducibility of the nanoindentation measurements. For instance, if one considers the E and H values of the AZ31 Mg alloy measured at 200 nm, comparing this sample finely-polished down to 1 μm diamond paste to another roughly-polished with P1200 SiC foil, the percentage errors change from 2.4% to 41.4% for the E value and from 4.4% to 61.0% for the H value. The data below 100 nm depth is subject to even larger variations. This also means that attempts to measure the E and H values of the thinner H30 films were unsuccessful and this paper focuses on the 100 h films.

The E and H values obtained at a 200 nm depth and corresponding p-values from pair comparisons are shown in Fig. 7 and Table 2. It can be seen that the H100 film is harder than the AZ31 substrate, as the differences between the two samples are statistically significant (p-value$<$0.05), despite the significant error values. Coating the AZ31 with the H100 film produces a small loss of stiffness E (from 52.4 to 39.7 GPa), an obvious hardening effect (from 1.06 to 1.89 GPa) and, crucially, very large increases in elastic strain at break H/E (from 2.07 $\times$ 10^{-2} to 5.23

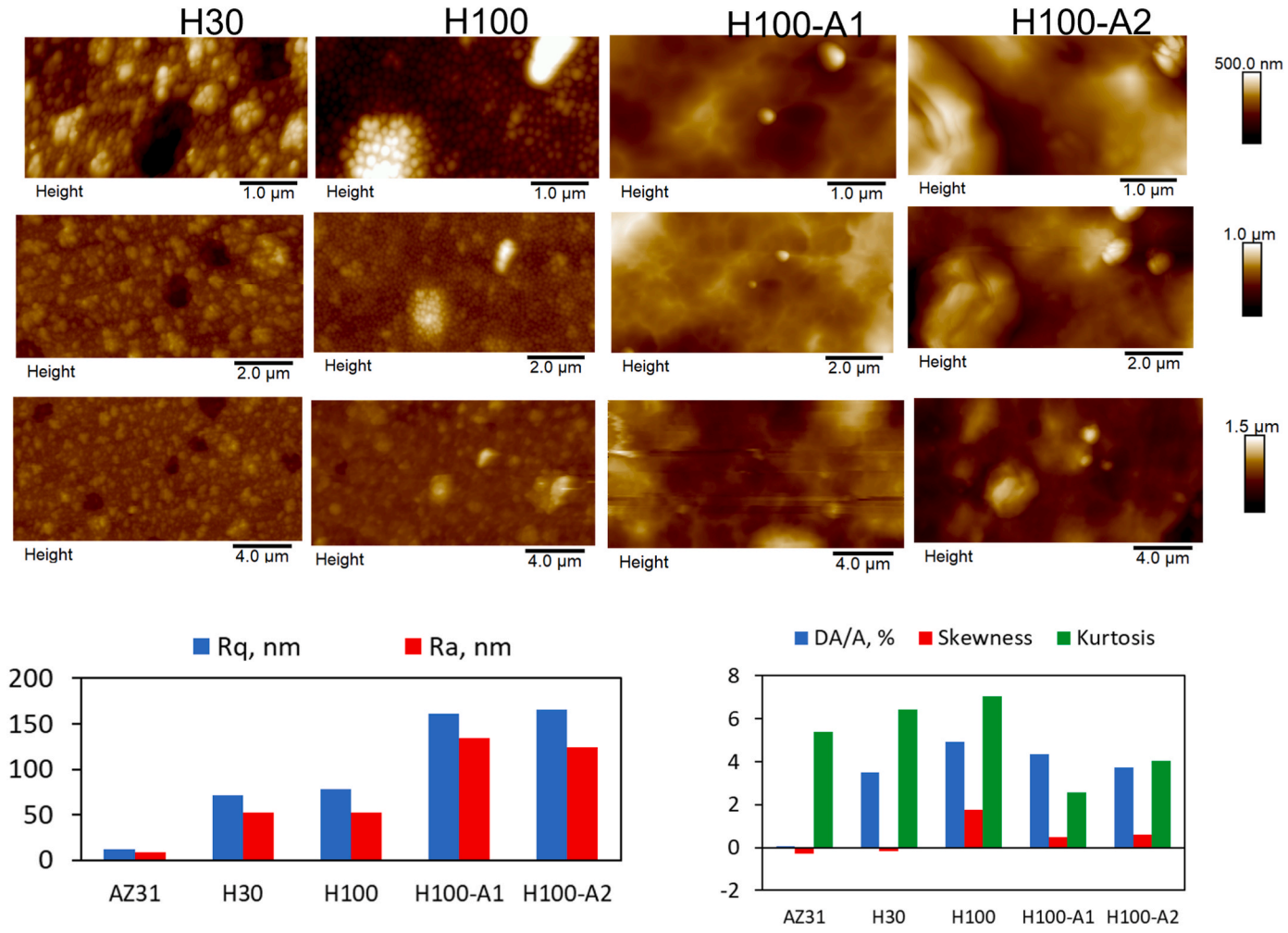

Fig. 5. TAFM micrographs of the AZ31 substrate and the HA films with bar charts of the roughness values (R_q and R_a), specific surface area (DA/A in %), skewness and kurtosis.

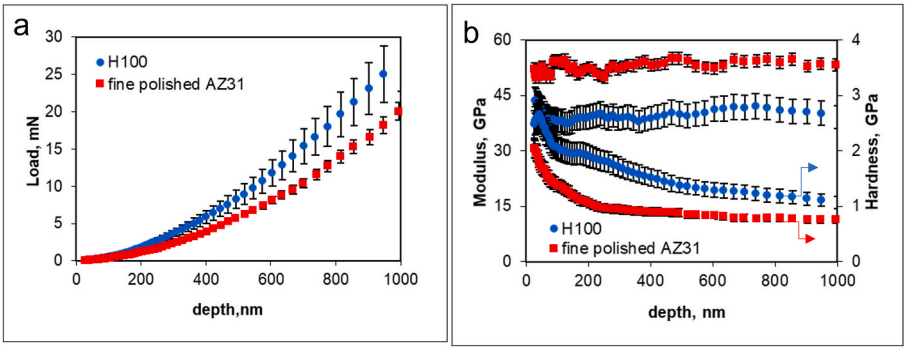

Fig. 6. Nanoindentation Load-displacement curve (a) and Hardness and Modulus curves (b) for a 1 μm diamond polished AZ31 Mg alloy and a H100 film deposited on it.

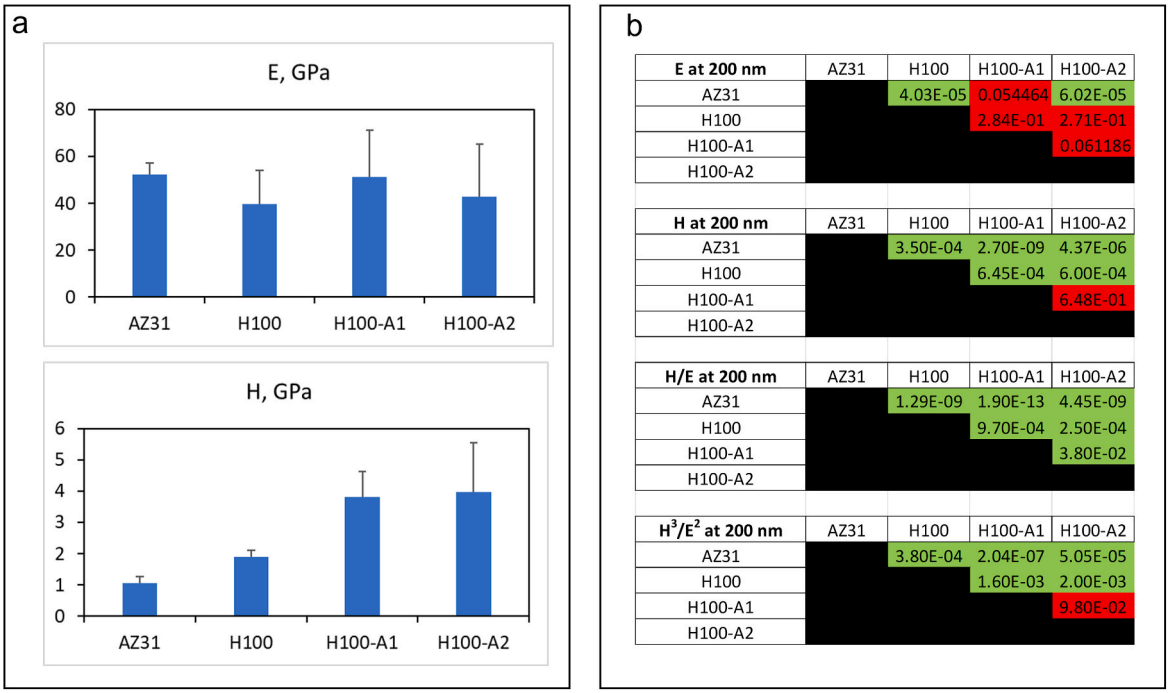

E at 200 nm	AZ31	H100	H100-A1	H100-A2
AZ31		4.03E-05	0.054464	6.02E-05
H100			2.84E-01	2.71E-01
H100-A1				0.061186
H100-A2				

H at 200 nm	AZ31	H100	H100-A1	H100-A2
AZ31		3.50E-04	2.70E-09	4.37E-06
H100			6.45E-04	6.00E-04
H100-A1				6.48E-01
H100-A2				

H/E at 200 nm	AZ31	H100	H100-A1	H100-A2
AZ31		1.29E-09	1.90E-13	4.45E-09
H100			9.70E-04	2.50E-04
H100-A1				3.80E-02
H100-A2				

H^3/E^2 at 200 nm	AZ31	H100	H100-A1	H100-A2
AZ31		3.80E-04	2.04E-07	5.05E-05
H100			1.60E-03	2.00E-03
H100-A1				9.80E-02
H100-A2				

Fig. 7. Bar charts of E and H values for the various samples calculated at 200 nm depth. The table gathers the p-values for pair comparisons of E, H, H/E and H^3/E^2 (a green cell means p-value<0.05, a red cell p-value>0.05).

Table 2
Nanoindentation results; the measured values at 200 nm depth together with those extracted from the Bhattcharya model (Fig. 8 (Bhattcharya and Nix, 1998),). The values in parenthesis are the R^2 coefficient of the fit to the data.

	measured at 200 nm depth				film values from model			
sample	**E, GPa**	**H, GPa**	**H/E**	**H^3/E^2, GPa**	**E, GPa (R^2)**	**H, GPa (R^2)**	**H/E**	**H^3/E^2, GPa**
AZ31	52.4 ± 4.9	1.06 ± 0.22	2.07E-02	4.80E-04	–	–	–	–
H100	39.7 ± 14.8	1.89 ± 0.83	5.23E-02	8.66E-03	63 (0.971)	2.7 (0.971)	4.29E-02	4.96E-03
H100-A1	51.4 ± 19.7	3.81 ± 1.57	7.99E-02	2.64E-02	90.4 (0.966)	6.92 (0.995)	7.65E-02	4.05E-02
H100-A2	42.8 ± 21.2	3.98 ± 2.06	1.11E-01	4.64E-02	119.5 (0.993)	9.4 (0.994)	7.87E-02	5.82E-02

$\times 10^{-2}$) and resistance to plastic deformation H^3/E^2 (from 4.98×10^{-4} to 8.66×10^{-2}), suggesting a significant toughening of the surface. Similar results were found for HA films prepared by RF-magnetron sputtering in grounded and negative-bias conditions (Surmeneva et al., 2015), although in that study the thickness was only given for the bias condition. Indeed, comparing nanoindentation results for films of different thickness is difficult because of the substrate effect. To gauge the influence of this substrate effect, the E(h) and H(h) curves for the H100 coating were fitted to the Bhattcharya model (Bhattcharya and Nix, 1998), for depths larger than 100 nm, and the results are shown in Fig. 8 and Table 2. The improvements in intrinsic film properties are even larger. Results for the annealed samples are also displayed in Fig. 8. Annealing brings further improvements of H, H/E and H^3/E^2, as measured at 200 nm depth. It should be noted that the E and H values measured in this study are within the range of previously published values for nanoindentation studies of HA films, although these published values vary significantly as they cover a range of deposition techniques, conditions and nanoindentation measurement conditions. Even,

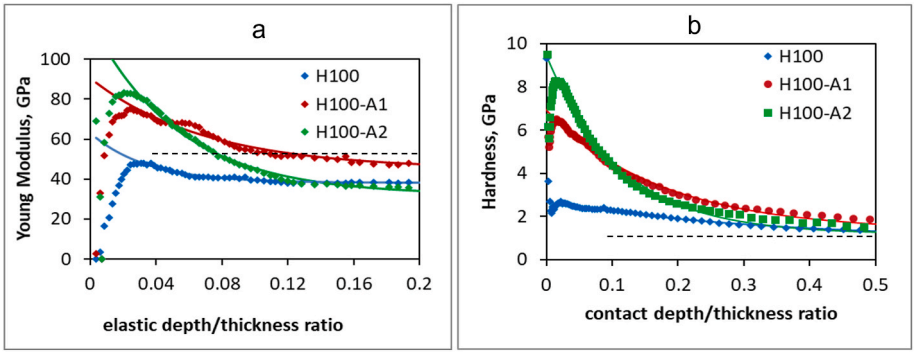

Fig. 8. Nanoindentation results, (a) Young's modulus (E) and (b) hardness (H) curves for samples H100, H100-A1 and H100-A2. The x-axis scales with depth and is, for the E curve, $b_e = h_e/t$ the ratio of elastic depth over film thickness and, for the H curve b_c, the ratio of contact depth h_c over film thickness. The large depth E and H value of the AZ31 Mg substrate are indicated with the black dashed lines and the fit to the Batcharnaya model (ref. 21) is shown with the coloured lines.

restricting oneself to RF magnetron sputtering, the published reviews of nanoindentation data on HA films (Surmenev, 2012; Ben-Nissan et al., 2013) find E and H values varying, respectively, from 78 to 155 GPa and 3.4–10 GPa, because of the influence of deposition conditions, film thickness and depth of measurement. Our measurements of intrinsic film properties, determined by the model, are also shown in Table 2. These intrinsic E and H film values have been determined for the annealed films (90.4 GPa and 6.92 GPa, respectively for H100-A1 and 119.5 GPa and 9.40 GPa, respectively for H100-A2) are in line with those published in one of our previous study using the same film model (respectively 130 GPa and 7.5 GPa) (Lubarsky et al., 2014). This is striking as the two studies used films with different thickness (1000 nm and 500 nm), different substrates (AZ31 Mg alloy and Ti) and different annealing procedure (IR flash annealing and oven annealing) and this validates the approach taken giving film values without influence from the substrate or film thikcness. These findings also agree with previous studies which have found that crystalline HA has higher Young's modulus and hardness than amorphous HA (Dinda et al., 2009). One should note that, although the elastic strain at break (H/E) values seem high for a ceramic coating, there are in line with previously published data (Surmeneva et al., 2015) and may also be an indication of the incomplete crystallization of the film, as suggested above. Comparing the H100-A1 and H100-A2 samples, we note higher intrinsic film E and H values for the H100-A2 film.

Results from constant load scratch experiments are shown in Fig. 9. Fig. 9 (a) shows the pre-scratch and post scratch profiles, with the plastic residual depth (or wear depth) indicated by the green double arrow for a single position of the AZ31 profile. The wear depths averaged over the track length are displayed in the bar chart of Fig. 9 (b). The H30 and H100 coatings are clearly more wear resistant than AZ31, with H100 being more wear-resistant than H30. However, annealing does not bring any measurable improvement in wear depth. The innocuity of Mg wear debris was commented on earlier on. However, worn marks on Mg alloys implants can lead to pitting corrosion and exacerbate the already high corrosion rate observed for these alloys. Hence the reduced wear observed for the coated alloys represents a real advantage for their use as bone implants.

Details of the scratches on H100 are shown in Fig. 10. Fig. 10 (a) indicates that the wear tracks have a pore-free and smooth interior. AFM cross-sections and FESEM micrographs (Fig. 10(b–d)) also show a smaller semi-apex angle (34°) for the scratch profile than for the diamond tip (45°), as measured by FESEM. This is indicative of an elastic spring-back of the deformation during scratch.

Considering that the blunting of the cube corner diamond scratch tip (Fig. 10 (d)) is much smaller than the wear depths measured, we can estimate the volumetric wear rate for the samples, approximating the tip

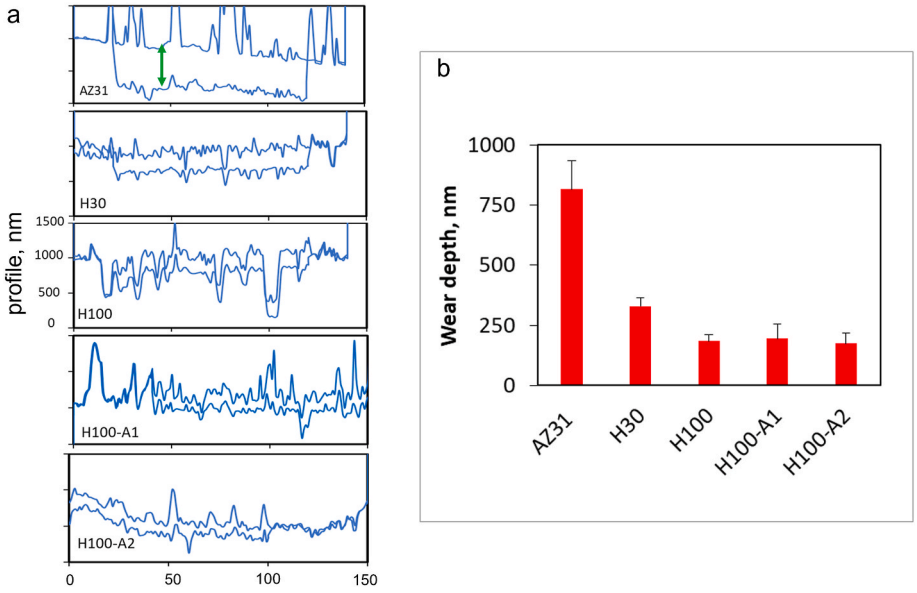

Fig. 9. (a)Nano-scratch profiles for the AZ31 and the various coatings for a 1 mN constant load edge forward test, same x, and y scales for all samples, (b)bar chart of average wear depths.

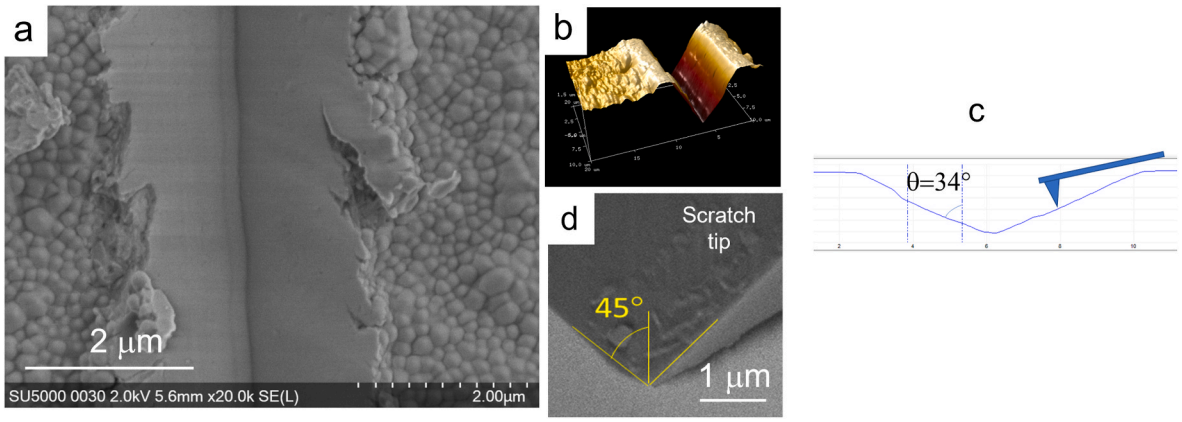

Fig. 10. (a) FESEM of a constant scratch on H100 showing a smooth, poor-free interior, (b) 3D AFM image and (c) AFM cross-section of scratch profile and (d) FESEM of the diamond scratch cube corner tip showing the elastic spring back during scratch.

as a sharp indenter. Taking the 1 mN data, we find a wear rate of 0.66 mm^3/N.m for AZ31 and varying between 0.03 and 0.1 mm^3/N.m for the HA coatings. These values are higher than measured in a previously published scratch testing study of magnetron sputtered HA films on AZ31 Mg alloy ($4x10^{-5}$-$4x10^{-3}$ mm^3/N.m (Dinu et al., 2017). We believe that this discrepancy is due to this previous study using a much larger counter-body; a 6 mm diameter sapphire ball. Taking into account the loads used in the two studies (1N and 1 mN), and using Hertz contact mechanics, gives contact pressure P_c of 41 MPa and 2 GPa for this previous study and our study, respectively. As the onset of plasticity and crack propagation, and therefore the wear rate, all respond to P_c (Gu et al., 2021; Tayebi and Polycarpou, 2004), this accounts for the observed differences in wear rates. We observed a similar effect in a previous nano-scratch testing study of amorphous carbon films (Lemoine et al., 2004). Despite this, these measurements show that these HA coatings improve the tribological performances of the Mg alloy.

However, conducting wear depth measurements on rough samples is challenging as roughness and topographic features have a significant influence on friction (Stanford and Jain, 2001) and wear (Kennedy et al., 2003) and results in large standard deviations in measured wear depth. An alternative approach is to look at the width of the wear tracks, easily measured from top view FESEM micrographs, as these measurements are minimally influenced by roughness. Examples are shown in Fig. 11 for both edge-forward and face-forward constant load scratch experiments. Although the edges of the scratches formed in the face-forward configuration are relatively smooth, for the edge-forward case, one notes the appearance of serrated edges and separated chips on the edge of the tracks. This has been observed before and attributed to the greater densification deformation in the edge-forward case (Wan et al., 2020). In both configurations the H100 track width is smaller than that of the AZ31 and annealing seem to decrease further the track width. From the measurement of these track widths, a scratch hardness H_S (Karimzadeh et al., 2014) can be defined as;

$$H_S = 2.31\,\frac{L}{w^2} \tag{4}$$

where L is the normal load and w the track width.

A bar chart of these H_S values is shown in Fig. 12 (a). The tables shown in Fig. 12 (b) represent the student t-test p-values for every pair comparison. It shows that in most cases, every pair comparison is statistically significantly different. Examining these differences, we find that the H_S value of H100 is higher than that of AZ31, as observed in Fig. 9. Fig. 12 also shows that annealing increases the H_S value and that H100-A1 has a larger H_S value than H100-A2, two observations which could not be made by measuring the wear depths.

To investigate this further, coating/substrate delaminations were

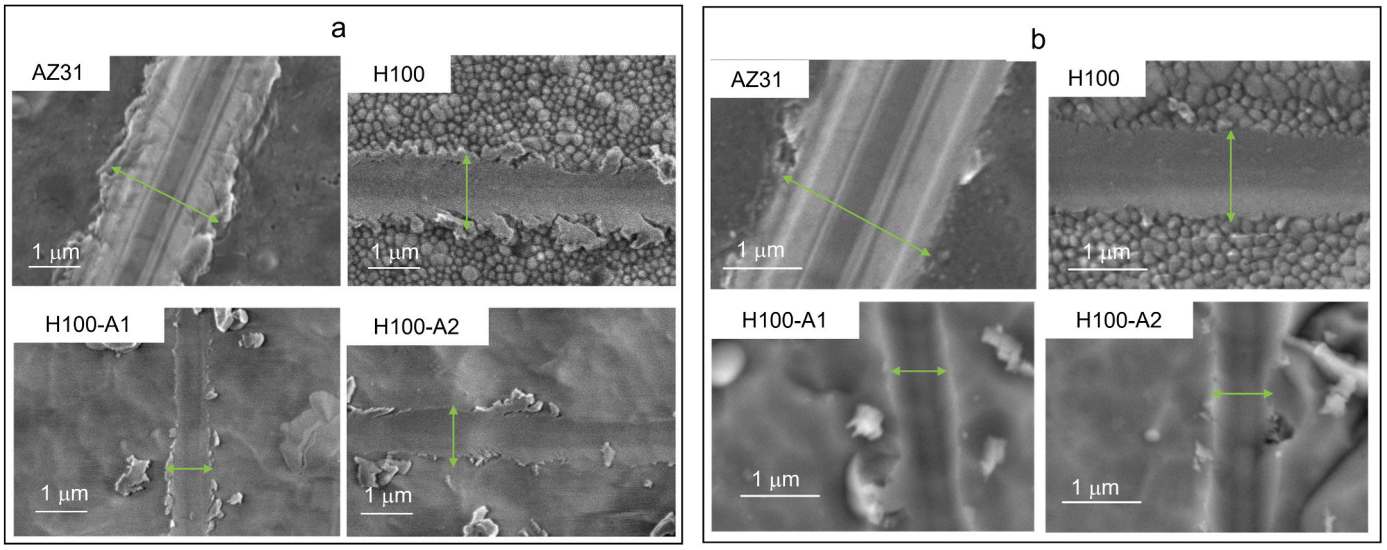

Fig. 11. FESEM micrographs at 2 kV of wear tracks done at 1 mN in (a) the edge forward and (b) the face-forward configuration. The micron bar for all micrographs is 1 μm. The green arrows show the track width.

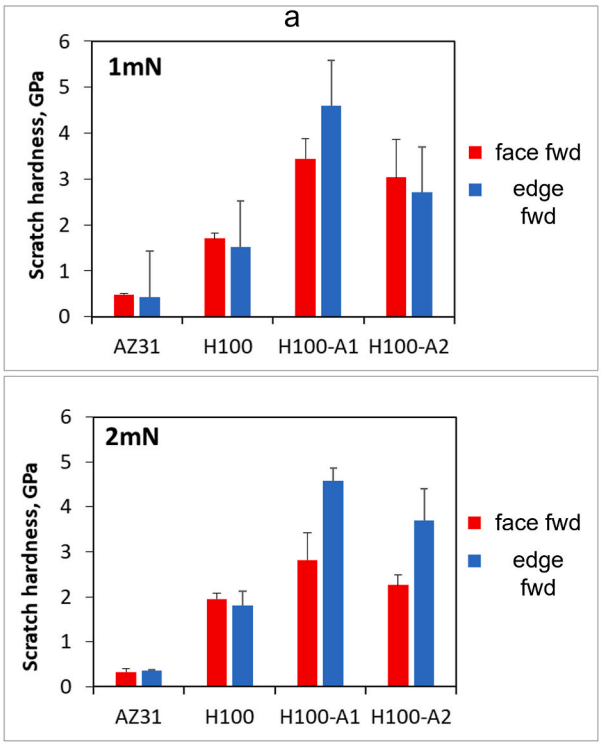

b

1mN face fwd	AZ31	H100	H100-A1	H100-A2
AZ31		5.30E-10	6.30E-07	7.60E-05
H100			3.60E-07	1.20E-03
H100-A1				0.378
H100-A2				

1mN edge fwd	AZ31	H100	H100-A1	H100-A2
AZ31		1.30E-03	1.30E-03	2.70E-04
H100			1.20E-05	1.80E-04
H100-A1				2.00E-03
H100-A2				

2mN face fwd	AZ31	H100	H100-A1	H100-A2
AZ31		9.20E-09	5.50E-05	1.10E-09
H100			3.40E-03	7.20E-03
H100-A1				1.00E-02
H100-A2				

2mN edge fwd	AZ31	H100	H100-A1	H100-A2
AZ31		2.20E-07	3.70E-12	6.10E-07
H100			4.30E-09	6.70E-05
H100-A1				4.50E-02
H100-A2				

Fig. 12. (a) Bar charts of scratch hardness (H_S) from constant load nano-scratch tests at 1 mN and 2 mN and (b) table of p-values for pair comparisons (a green cell means p-value<0.05, a red cell p-value>0.05).

investigated with ramping load scratch testing. Fig. 13 (a) shows an SEM micrograph and corresponding EDX map of the final section of the scratch profiles on a H100 sample for various scratch conditions (final load 20–100 nN, 1–10 μm/s) with critical load (L_c) shown in white on the Ca map; i.e., corresponding to the appearance of the Ca count on the Ca map. Note that, in this case, the FESEM micrograph is slightly shifted with respect to the corresponding EDX maps and that these micrographs only represent the final section of those ramping load scratches. Despite the large variations in film's topography and the wide range of ramping scratch loads and speeds, the L_c values are over a relatively narrow range

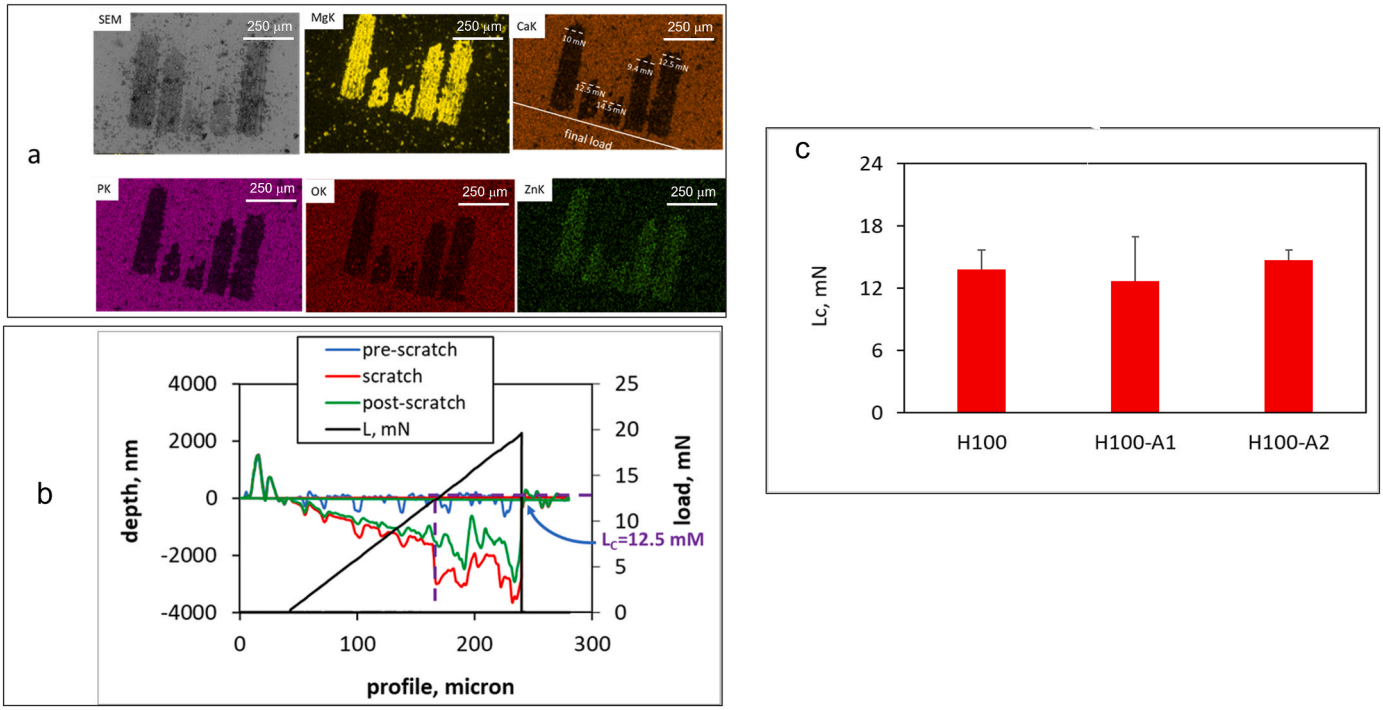

Fig. 13. Ramping load nano-scratch experiments showing (a) an SEM micrograph and corresponding EDX map of the final section of the scratch profiles on a H100 sample for various scratch conditions (final load 20–100 nN, 1–10 μm/s) with critical load for delamination (L_c) shown in white on the Ca map. (b) a scratch profile and load ramp with critical load L_c for a H100 sample tested up to 20 mN and (c) bar chart of L_c values for H100, H100-A1 and H100-A2 films.

of 9.4–14.5 mN (average 12 mN ± 2.6 mN; i.e., 22% rel. error). Fig. 13 (b) shows the scratch profile for the 20 mN condition of Fig. 13 (a) and here the L_c value is defined as the load at which the profile suddenly changes (12.5 mN in this case). This corroboration permits to identify those L_c values as indeed the critical load for film delamination. Similar experiments carried out on a H30 sample gives a L_c value of 2–5 mN, much harder to define for this thinner film but distinctly smaller than for the thicker H100 film. This decrease in critical load is expected; as previous measurements (Roy et al., 2010) on SiCN films have shown that L_c decreases with film thickness; as the film thickness decreases less load is required to produce the same deformation at the film/substrate interface (Kennedy et al., 2003). Finally, Fig. 13 (c) indicate that annealing the H100 films did not change the value of the critical load significantly; meaning the annealing treatment did not compromise the interfacial strength of the HA/AZ31 system. Finally, it should be appreciated, as noted in several comprehensive reviews of nano-scratch testing (Beake et al., 2013; Bull and Berasetegui, 2006), that it is difficult to quantitatively link the value of the critical load L_c to σ, the interfacial shear strength of the film/substrate interface, firstly because the analytical link between L_c and σ depends on the nature of the failure mode, not always known and, secondly because not all of the stored elastic deformation energy is used to open that interface. Indeed, in the scratch profiles of Fig. 13, most of the deformation before L_c is plastic.

4. Conclusions

This nanotribological study has shown that magnetron-sputtered HA films on AZ31 magnesium alloys result in rougher surfaces. Despite this unfavourable tribological situation, the coated alloys are harder and tougher surfaces and show improved wear resistance during scratching. In particular, this investigation extracted the intrinsic film nano-mechanical properties of the films, an indispensable perquisite for carrying out an FEA analysis of the insertion of coated bone implants. In addition, EDX and XRD analysis indicate that as-deposited coatings are amorphous and Ca-deficient whereas rapid thermal annealing results in c-axis orientation and near-stoichiometric composition. More work is in progress to control and minimize defects in the film and to use such tribological data to help model the insertion of HAP-coated implants into bone. Nevertheless, this investigation shows that low temperature flash annealing enhances the potential of bone fracture fixation devices fabricated from resorbable HA coated Mg alloys to withstand the forces associated with surgical implantation.

CRediT authorship contribution statement

Patrick Lemoine: Writing – review & editing, Writing – original draft, Validation, Methodology, Investigation, Data curation, Conceptualization. **Jonathan Acheson:** Writing – review & editing, Validation, Investigation, Data curation. **Stephen McKillop:** Writing – review & editing, Investigation. **Jeroen JJP. van den Beucken:** Writing – review & editing, Investigation. **Joanna Ward:** Writing – review & editing, Project administration, Data curation. **Adrian Boyd:** Writing – review & editing, Investigation. **Brian Meenan:** Writing – review & editing, Funding acquisition.

Declaration of competing interest

The authors declare that they have no known competing financial interests or personal relationships that could have appeared to influence the work reported in this paper.

Acknowledgments

Authors would like to acknowledge the Department for Economy (DfE), Northern Ireland for funding of the US-Ireland Centre-to-Centre partnership associated with this work (USI 111). Support of the United States NSF-ERC (Grant No. EEC-0812348) is also acknowledged.

References

Acheson, J.G., McKillop, S., Lemoine, P., Boyd, A.R., Meenan, B.J., 2019. Mater 6. https://doi.org/10.1016/j.mtla.2019.100291.
Acheson, J.G., McKillop, S., Ward, J., Roy, A., Xu, Z., Boyd, A.R., Lemoine, P., Kumta, P. N., Sankar, J., Meenan, B.J., 2021. Surf. Coating. Technol. 421 https://doi.org/10.1016/j.surfcoat.2021.127446.
Acheson, J.G., Gallagher, E.A., Ward, J., McKillop, S., FitzGibbon, B., Boyd, A.R., Meenan, B.J., Lemoine, P., McGarry, J.P., 2022. Surf. Coating. Technol. 429 https://doi.org/10.1016/j.surfcoat.2021.127944.
Ahmed, H.S.T., Jankowski, A.F., 2011. Thin Solid Films 520, 1516. https://doi.org/10.1016/j.tsf.2011.06.004.
Antoniac, I., Adam, R., Biță, A., Miculescu, M., Trante, O., Petrescu, I.M., Pogărășteanu, M., 2021. Mater 14, 1. https://doi.org/10.3390/mH100-A14010084.
Banday, S., Reshi, B.A., Wani, M.F., 2021. Ceram. Int. 47, 35260 https://doi.org/10.1016/j.ceramint.2021.09.068.
Bazhenov, V.E., Li, A.V., Komissarov, A.A., Koltygin, A.V., Tavolzhanskii, S.A., Bautin, V. A., Voropaeva, O.O., Mukhametshina, A.M., Tokar, A.A., 2021. J. Magnes. Alloys 9, 1428. https://doi.org/10.1016/j.jma.2020.11.008.
Beake, B.D., Harris, A.J., Liskiewicz, T.W., 2013. Tribol. Mater. Surface Interfac. 7, 87. https://doi.org/10.1179/1751584X13Y.0000000037.
Ben-Nissan, B., Choi, A.H., Bendavid, A., 2013. Surf. Coating. Technol. 233, 39. https://doi.org/10.1016/j.surfcoat.2012.11.020.
Bhattcharya, A.K., Nix, W.D., 1998. Int. J. Solid Struct. 24, 1287. https://doi.org/10.1016/0020-7683(88)90091-1.
Borcherding, K., Schmidmaier, G., Hofmann, G.O., Wildemann, B., 2021. Injury 52, S106. https://doi.org/10.1016/j.injury.2020.11.050.
Boyd, A.R., O'Kane, C., O'Hare, P., Burke, G.A., Meenan, B.J., 2013. J. Mater. Sci. Mater. Med. 24, 2845. https://doi.org/10.1007/s10856-013-5021-3.
Bull, S.J., Berasetegui, E.G., 2006. Tribol. Int. 39, 99. https://doi.org/10.1016/j.triboint.2005.04.013.
Dinda, G.P., Shin, J., Mazumder, J., 2009. Acta Biomater. 5, 1821. https://doi.org/10.1016/j.actbio.2009.01.027.
Dinu, M., Ivanova, A.A., Surmeneva, M.A., Braic, M., Tyurin, A.I., Braic, V., Surmenev, R. A., Vladescu, A., 2017. Ceram. Int. 43, 6858. https://doi.org/10.1016/j.ceramint.2017.02.106.
Esmaily, M., Svensson, J.E., Fajardo, S., Birbilis, N., Frankel, G.S., Virtanen, S., Arrabal, R., Thomas, S., Johansson, L.G., 2017. Prog. Mater. Sci. 89, 92. https://doi.org/10.1016/j.pmatsci.2017.04.011.
Fernandes, K.R., Zhang, Y., Magri, A.M.P., Renno, A.C.M., Van Den Beucken, J.J.J.P., 2017. ACS Biomater. Sci. Eng. 3, 3318. https://doi.org/10.1021/acsbiomaterials.7b00679.
Gu, C., Meng, X., Wang, S., Ding, X., 2021. Proc. Inst. Mech. Eng. Part J Eng Tribol 235, 256. https://doi.org/10.1177/1350650120940211.
He, L.Y., Zhang, X.M., Liu, B., Tian, Y., Ma, W.H., 2016. Braz. J. Med. Biol. Res. 49 https://doi.org/10.1590/1414-431X20165257.
Howell, P.G.T., Davy, K.M.W., Boyde, A., 1998. Scanning 20, 35. https://doi.org/10.1002/sca.1998.4950200105.
Kanaya, K., Okayama, S., 1972. J. Phys. D 5, 43. https://doi.org/10.1088/0022-3727/5/1/308.
Karimzadeh, A., Ayatollahi, M.R., Bushroa, A.R., Herliansyah, M.K., 2014. Ceram. Int. 40, 9159. https://doi.org/10.1016/j.ceramint.2014.01.131.
Kennedy, F.E., Lidhagen, D., Erdemir, A., Woodford, J.B., Kato, T., 2003. Wear 255, 854. https://doi.org/10.1016/S0043-1648(03)00223-0.
Lemoine, P., Zhao, J.F., Quinn, J.P., McLaughlin, J.A., Maguire, P., 2000. Thin Solid Films 379, 166. https://doi.org/10.1016/S0040-6090(00)01543-1.
Lemoine, P., Quinn, J.P., Maguire, P., McLaughlin, J.A., 2004. Wear 257, 509. https://doi.org/10.1016/j.wear.2004.01.010.
Lemoine, P., Quinn, J.P., Maguire, P.D., Zhao, J.F., McLaughlin, J.A., 2007. Appl. Surf. Sci. 253, 6165. https://doi.org/10.1016/j.apsusc.2007.01.028.
Lilley, K.J., Gbureck, U., Knowles, J.C., Farrar, D.F., Barralet, J.E., 2005. J. Mater. Sci. Mater. Med. 16, 455. https://doi.org/10.1007/s10856-005-6986-3.
Lubarsky, G.V., Lemoine, P., Meenan, B.J., Deb, S., Mutreja, I., Carolan, P., Petkov, N., 2014. Mater. Res. Express 1. https://doi.org/10.1088/2053-1591/1/2/025404.
Luffy, S.A., Chou, D.-, Waterman, J., Wearden, P.D., Kumta, P.N., Gilbert, T.W., 2014. J. Biomed. Mater. Res. 102, 611. https://doi.org/10.1002/jbm.a.34731.
Ma, X., Ma, J., Bian, X., Tong, X., Han, D., Jia, Y., Wu, S., Zhang, N., Geng, C., Li, P., Wang, Q., Zhang, Y., Wang, G., 2021. Inter 133. https://doi.org/10.1016/j.intermet.2021.107159.
Markhoff, J., Grabow, N., 2020. Curr. Dir. Biomed. Eng. 6 https://doi.org/10.1515/cdbme-2020-3112.
Muller, R.H., 1954. Phys. Rev. 93, 891–892. https://doi.org/10.1103/PhysRev.93.891.2.
Oliver, W.C., Pharr, G.M., 1992. J. Mater. Res. 7, 1564.
Roy, S., Darque-Ceretti, E., Felder, E., Raynal, F., Bispo, I., 2010. Thin Solid Films 518, 3859. https://doi.org/10.1016/j.tsf.2010.02.004.
Shuai, C., Wang, B., Yang, Y., Peng, S., Gao, C., 2019. Compos. B Eng. 162, 611. https://doi.org/10.1016/j.compositesb.2019.01.031.
Stanford, M.K., Jain, V.K., 2001. Wear 250-251, 990. https://doi.org/10.1016/S0043-1648(01)00719-0.
Surmenev, R.A., 2012. Surf. Coating. Technol. 206, 2035. https://doi.org/10.1016/j.surfcoat.2011.11.002.

Surmenev, R.A., Surmeneva, M.A., Evdokimov, K.E., Pichugin, V.F., Peitsch, T., Epple, M., 2011. Surf. Coating. Technol. 205, 3600. https://doi.org/10.1016/j.surfcoat.2010.12.039.

Surmeneva, M.A., Surmenev, R.A., Nikonova, Y.A., Selezneva, I.I., Ivanova, A.A., Putlyaev, V.I., Prymak, O., Epple, M., 2014. Appl. Surf. Sci. 317, 172. https://doi.org/10.1016/j.apsusc.2014.08.104.

Surmeneva, M.A., Tyurin, A.I., Mukhametkaliyev, T.M., Pirozhkova, T.S., Shuvarin, I.A., Syrtanov, M.S., Surmenev, R.A., 2015. J. Mech. Behav. Biomed. Mater. 46, 127. https://doi.org/10.1016/j.jmbbm.2015.02.025.

Takahashi, K., Van Den Beucken, J.J.J.P., Wolke, J.G.C., Hayakawa, T., Nishiyama, N., Jansen, J.A., 2008. J. Biomed. Mater. Res. 84, 682. https://doi.org/10.1002/jbm.a.31341.

Tayebi, N., Polycarpou, A.A., 2004. Tribol. Int. 37, 491. https://doi.org/10.1016/j.triboint.2003.11.010.

Wan, Z., Wang, W., Feng, J., Dong, L., Yang, S., Jiang, Z., 2020. Ceram. Int. 46, 16754 https://doi.org/10.1016/j.ceramint.2020.03.251.

Won, S., Huh, Y.-, Cho, L.-, Lee, H.-, Byon, E.-, Park, C.-, 2017. Tissue Eng. Regen. Med. 14, 123. https://doi.org/10.1007/s13770-017-0028-3.

Yan, X., Chen, L., Xu, X., Zhao, Y., Zhao, M., 2021. Adv. Eng. Mater. https://doi.org/10.1002/adem.202100396.

Yoshinari, M., Hayakawa, T., Wolke, J.G.C., Nemoto, K., Jansen, J.A., 1997. J. Biomed. Mater. Res. 37, 60. https://doi.org/10.1002/(SICI)1097-4636(199710)37:1<60::AID-JBM8>3.0.CO;2-H.

Yoshizawa, S., Brown, A., Barchowsky, A., Sfeir, C., 2014. Acta Biomater. 10, 2834. https://doi.org/10.1016/j.actbio.2014.02.002.

Yuan, H., Fernandes, H., Habibovic, P., De Boer, J., Barradas, A.M.C., De Ruiter, A., Walsh, W.R., Van Blitterswijk, C.A., De Bruijn, J.D., 2010. Proc. Natl. Acad. Sci. U. S. A. 107, 13614 https://doi.org/10.1073/pnas.1003600107.

Zhi, X., Li, X., Yuan, S., Wang, D., Wang, K., 2022. Optik 251. https://doi.org/10.1016/j.ijleo.2021.168404.